Immunometabolic profiling of *in vitro* and *ex vivo Leishmania*-infected macrophages (LIMs) reveals unique polarization and bioenergetic signatures

Sheng Zhang[1], Hervé Lecoeur[1], Hugo Varet[2, 3], Rachel Legendre[2, 3], Nassim Mahtal[4], Caroline Proux[3], Nathalie Aulner[4], Spencer Shorte[4], Capucine Granjean[5], Philippe Bousso[5], Eric Prina[1], and Gerald F. Späth[1]

[1]Institut Pasteur, Université Paris Cité, INSERM U1201, Unité de Parasitologie moléculaire et Signalisation, Département des Parasites et Insectes vecteurs, 25 Rue du Dr Roux, 75015 Paris, France; [2]Institut Pasteur, Université Paris Cité, Hub Bioinformatique et biostatistique, 28 Rue du Dr Roux, 75015 Paris, France ; [3]Institut Pasteur, Université Paris Cité, Plate-forme Technologique Biomics, Centre de Ressources et Recherches Technologiques (C2RT), 28 Rue du Dr Roux, 75015 Paris, France; [4]Institut Pasteur, Université Paris Cité, Unité de Technologie et service Biolmagerie Photonique (UtechS PBI), 25 Rue du Dr Roux, 75015 Paris, France; [5]Institut Pasteur, Université Paris Cité, Unité Dynamique des réponses immunes, 25 Rue du Dr Roux, 75015 Paris, France.

*Correspondence: gerald.spaeth@pasteur.fr

Keywords: Macrophage, *Leishmania*, metabolism, polarization, transcriptome

sheng.zhang@pasteur.fr, herve.lecoeur@pasteur.fr, hugo.varet@pasteur.fr, rachel.legendre@pasteur.fr, nassim.mahtal@pasteur.fr, caroline.proux@gmail.com, nathalie.aulner@pasteur.fr, spencer.shorte@pasteur.fr, capucine.grandjean@pasteur.fr, philippe.bousso@pasteur.fr, eric.prina@pasteur.fr, gerald.spaeth@pasteur.fr

ABSTRACT

Macrophages are the major host cells of the protozoan parasite *Leishmania* in mammalian infection. These key innate immune cells display remarkable phenotypic plasticity ranging from pro-inflammatory M1 to anti-inflammatory M2 macrophages that can control infection and tissue homeostasis, respectively. It has been recognized that *Leishmania* exploits macrophage phenotypic plasticity to establish chronic infection. However, the current notion that these parasites simply trigger an M2-like phenotype seems over-simplified considering the immunopathology observed during leishmaniasis, is which often characterized by a mixed Th1/Th2 immune response. Here we combined a series of systems-level analyses to shed new light on the phenotype of *Leishmania*-infected macrophages (LIMs). Immunometabolic profiling by RNAseq, quantitative RT-qPCR, cytokine immunoassays, and bioenergetic flux analysis of *Leishmania amazonensis*-infected bone marrow-derived macrophages (BMDMs) revealed a highly complex, mixed polarization phenotype and a unique bioenergetic signature. *In vitro* LIMs were characterized by (i) co-expression of both M1 and M2 markers at RNA and protein levels, (ii) expression changes of a unique set of inflammatory genes (e.g. RELA, IGFBP3, VEGFA), and (iii) modulation of metabolic gene expression, including up regulation of glycolytic genes. This LIMs-specific phenotype persisted for at least 30 days and was confirmed *in vivo* in lesion-isolated LIMs. Likewise, *in vitro* LIMs showed a mixed bioenergetic profile, increasing both glycolytic activity and oxidative phosphorylation (OXPHOS) compared to uninfected, nonpolarized macrophages (M0). Surprisingly, the elimination of intracellular parasites using the fast-acting, anti-leishmanial drug L-leucine-O-methyl ester (LME) enhanced both bioenergetic pathways to levels comparable to M1 (glycolysis) and M2 (OXPHOS) macrophages as soon as one hour after treatment, suggesting that *L. amazonensis* limits in real-time energy metabolism and ATP production in LIMs. In conclusion, *L. amazonensis* infection establishes a mixed, immunometabolomic polarization

profile in infected BMDMs and lesional macrophages that on one hand can promote an M1-regulated Th1 response required for the recruitment of new host cells to infected tissues, while at the same time promoting an M2 phenotype that dampens pro-inflammatory immune-signaling and shields intracellular parasites from leishmanicidal Nitric Oxide (NO).

INTRODUCTION

Intracellular pathogens have co-evolved strategies to neutralize anti-microbial activities of their host cells, harness their nutritional supplies and domesticate their metabolism to promote microbial survival and proliferation. The eukaryotic pathogen *Leishmania* represents an interesting model system to dissociate such immunometabolic subversion as these parasites infect and thrive inside important immune cells, including macrophages (Mφs) (Antonia and Ko, 2020; Bogdan, 2020; Lecoeur et al., 2022). These key innate immune cells display remarkable phenotypic plasticity that adapts their immune functions to local tissues and changes in the microenvironment. Indeed, Mφs can adopt a spectrum of polarization states ranging from canonical pro-inflammatory M1 cells that carry antimicrobial immune function and promote T helper type 1 responses, to anti-inflammatory M2 cells that promote T helper type 2 responses, and are associated with tissue homeostasis and wound-healing. Mφ polarization is driven by a complex interplay between extrinsic immune signals (cytokines/chemokines) and intrinsic metabolic signals. On one hand, M1 polarization is triggered by pro-inflammatory cytokines (e.g. IFNγ) and linked to induction of i) the glycolytic activity that rapidly generates ATP to support phagocytic and antimicrobial functions, ii) the Pentose Phosphate Pathway (PPP) that generates NADPH and supports ROS production via NADPH oxidase, iii) fatty acid synthesis, and ii) an interrupted Tricarboxylic Acid (TCA) cycle (Russell et al., 2019). On the other hand, M2 polarization is triggered by anti-inflammatory cytokines (e.g. IL4) and is associated with an intact TCA cycle, increased mitochondrial OXPHOS, increased fatty acid oxidation, and suppression of the PPP (Diskin and Palsson-McDermott, 2018).

The capacity of *Leishmania* to subvert Mφ immune functions has attracted considerable attention given its important role in causing the severe immunopathologies characteristic of leishmaniasis. Considering various parasite species, hosts (mouse, human), Mφ systems

(primary cells, cell lines) and infection methods (*in vitro*, *in vivo*), the prevailing model suggests that *Leishmania* triggers M2 polarization to establish permissive conditions for infection through the reduced expression of pro-inflammatory genes (iNOS, TNF, inflammasome components) and increased expression of arginase-1, IL-10 or CD206 (Kumar et al., 2018; Lecoeur et al., 2020). In contrast, the interaction of *Leishmania* with the host cell metabolisms and the impact of metabolic reprogramming on Mφ polarization is less investigated, even though M1 and M2 states have tailored metabolic profiles that support their divergent functions (Cohen and Mosser, 2013; Murray, 2017; O'Neill et al., 2016; Russell et al., 2019). *Leishmania* were shown to subvert various macrophage metabolic pathways during short-term infection *in vitro*, switching from an early glycolytic metabolism to oxidative phosphorylation (Moreira et al., 2015; Rabhi et al., 2012; Ty et al., 2019), modulating cholesterol and triglycerides homeostasis (Rabhi et al., 2012), and causing accumulation of lipid droplets (Rodriguez et al., 2017). However, no detailed information is available on how *Leishmania* fine-tunes the interplay between macrophage polarization state, immuno-expression, and metabolic functions. Furthermore, current studies rely exclusively on short-term, *in vitro* infection models that only poorly mimic the immunometabolomic state of chronically infected macrophages *in vivo* harboring hundreds of parasites (Lecoeur et al., 2020).

To overcome these limitations, we conducted integrative, immunometabolomic analyses *in vitro* following *L. amazonensis*-infected murine bone marrow- derived macrophages (BMDMs) for up to 30 days post-infection, and *ex vivo* using tissue Mφs recovered from infected lesions. Integration of transcriptomic, bioenergetic and proteomic profiles uncovered a previously under-appreciated, highly complex phenotype of *Leishmania*-infected macrophages (here termed LIMs) far from a stereotypic M2-like polarization state. We provide first evidence that chronically infected LIMs co-express M1 and M2 immuno-metabolic

features that not only mirror but may be at the origin of the equally complex T cell response observed during clinical *Leishmania* infection.

MATERIAL AND METHODS

Ethics statement. Six-week-old female C57BL/6 and Swiss *nu/nu* mice were purchased from Janvier (Saint Germain-sur-l'Arbresle, France). Rag2^{tm1Fwa} (Shinkai et al., 1992) were bred at the Institut Pasteur. All animals were housed in A3 animal facilities according to the guidelines of Institut Pasteur and the "Comité d'Ethique pour l'Expérimentation Animale" (CEEA) and protocols were approved by the "Ministère de l'Enseignement Supérieur; Direction Générale pour la Recherche et l'Innovation" under number #19683.

Isolation, culture, and polarization of bone marrow-derived macrophages. Bone marrow exudate cells were recovered from tibias and femurs of C57BL/6 mice and cultured in bacteriological Petri dishes (Greiner bio-one 664161) in DMEM medium (Gibco Life Technologies, 2140821) containing 10% FCS, 50 units/µg/ml of penicillin/streptomycin and 50 µM β-mercaptoethanol (referred to in the following as 'complete medium') and supplemented with 50 ng/ml of mouse recombinant colony-stimulating factor 1 (rm-CSF-1, ImmunoTools GmbH, Germany, 682087) (Lecoeur et al., 2020). After 6 days at 37°C in a 7.5% CO2 atmosphere, adherent Mφs were detached with 25 mM EDTA (Sigma, RNBB4346) in PBS, and seeded in a complete medium into different plastic cell culture supports, including i) tissue culture-treated Petri dishes (Falcon® 100 mm TC-treated Cell Culture Dish, OPTILUX 353003) for RNASeq, ii) 384-well plates (culture-treated, flat-optically clear bottom, Cell carrier plate, PerkinElmer) for morphological analyses on images acquired with the OPERA

Phenix automated spinning disk confocal imager, iii) tissue culture-treated 6-well plates (Corning Life Science, 353046) for RT-qPCR and Western blot analyses, and iv) in Seahorse XFe96 tissue culture microplates (Agilent, 102601-100) for metabolic flux analyses. Four hours after plating, Mφs were treated either with i) 50 ng/ml rm-CSF-1 during 3 days to generate M0 Mφs , ii) 50 ng/ml LPS (*E. coli* 0111:B4, Sigma-Aldrich L288) for 2 days then with 20 ng/ml INF-γ (ImmunoTools, 681588) for one day for M1 polarization, or iii) 50 ng/ml rm-CSF-1 plus 10 ng/ml IL-4 (ImmunoTools, 681680) and 10 ng/ml IL-13 (ImmunoTools, 681300) for 3 days for M2 polarization.

Isolation of *ex vivo* lesional macrophages from mouse footpads. *Ex vivo* lesional Mφs were isolated from footpad lesions of RAG2 knock-out mice inoculated with lesion-derived amastigotes 2 months earlier. Mice were euthanized by carbon dioxide inhalation, footpads were removed and placed in Digestion Buffer (DB) composed of 50 U/ml DNAse I (Sigma-Aldrich), 100 U/ml collagenase II (Sigma-Aldrich), 100 U/ml collagenase IV (Sigma-Aldrich) and 1 U/ml dispase II (Roche Applied Science) in DMEM and placed on a 100 µm cell strainer. Footpads were perfused with one ml of DB at different locations and maintained at 37°C for 30 minutes. This step was repeated two times. Macrophages were recovered and washed in PBS (centrifugation at 50 g, 10 min, 4 °C) before processing.

***Leishmania* isolation and BMDM infection.** mCherry transgenic, tissue-derived amastigotes of *Leishmania amazonensis* strain LV79 (WHO reference number MPRO/BR/72/M1841, *L. am*) were isolated from infected footpads of Swiss nude mice (Lecoeur et al., 2010). Amastigotes were added at a ratio of 4 parasites per Mφ, which allowed us to reach an infection efficiency of 95% infected BMDMs as estimated by fluorescence microscopy analysis of

Hoechst 33342- stained samples. Mφs were cultured at 34°C for three days (short-term infection) and up to 30 days (long-term infection). For some experiments, 2 mM of the leishmanicidal compound Leucine-O-methyl ester (LME, Sigma-Aldrich) and its mock control (ISO-LME, Sigma-Aldrich) was added to Mφs 1 hour before or during the bioenergetic flux analysis (Rabinovitch and Zilberfarb, 1988). Heat-killed parasites were obtained by exposure at 45°C for 20 minutes (Lecoeur et al., 2020).

Determination of the bioenergetic profile of macrophages. The Extracellular Acidification Rate (ECAR), the mitochondrial Oxygen Consumption Rate (OCAR), and the ATP production rate were quantified at 37°C using the Agilent Seahorse XF Real-Time ATP Rate Assay Kit (Agilent, 103592-100) with the Seahorse XFe96 analyzer. Following BMDM distribution in Seahorse XF96 tissue culture microplates, Mφs were either polarized into M1 or M2 or infected for 3 days at 34°C. OCR and ECAR were measured at 37°C in Seahorse XF DMEM medium (pH7.4, with 10 mM glucose, 2 mM L-glutamine, and 1 mM sodium pyruvate) (Agilent, 103680-100). 1.5 μM Oligomycin, an inhibitor of ATP synthase in the complex V of the mitochondrial electron transport chain (ETC), and 0.5 μM Rotenone/Antimycin A (Rot/AA), inhibitors respectively of complexes I and II of the ETC, were sequentially injected into each well after 18 min and 36 min of measurement, respectively. ATP-related parameters were also measured and include the rate of ATP production associated with i) the conversion of glucose to lactate in the glycolytic pathway (GlycoATP production rate), and ii) the oxidative phosphorylation in the mitochondria (mitoATP production rate) as measured by oxygen consumption. The total ATP production rate (sum of mitochondrial ATP and glycolytic ATP production rates) was calculated according to the manufacturer's instructions and normalized by cell number per well (Counting of Hoechst 33342-stained nuclei).

Quantification of nitrites. Nitrites in culture supernatants were quantified by colorimetry using the Griess assay kit (Thermo Fisher Scientific, G7921), according to the manufacturer's instructions.

Proteome Profiler Mouse XL Cytokine Array. Supernatants of Mφ cultures from 3 independent biological experiments were collected, pooled, and added to the membranes provided by the Proteome Profiler Mouse XL Cytokine Array (ARY028**,** Biotech, R&D systems) according to the manufacturer's instructions. Each analyte was detected in duplicate dot plots. Luminescence detection and quantification were performed by the ImageQuantTL software. Protein levels were expressed as Z-scores based on the relative expression of the M0 group (Yange Liu et al., 2020). Scripts for Heatmap and Venn diagrams of Z-scores were based on native graphical functions and run using R version 4.1.2 (R Core Team (2021) R: A Language and Environment for Statistical Computing. R Foundation for Statistical Computing, Vienna. https://www.R-project.org/).

Image acquisition with the OPERA. BMDMs at day 6 of CSF-1 induced differentiation were seeded in 384-well plates and polarized to M1 and M2 Mφs as described above, or infected with *L. amazonensis* lesion-derived amastigotes. On day 3 post-infection (PI) or polarization, Mφs were fixed and stained with Hoechst 33342 for nuclear staining, with PhenoVue™ Fluor 488-Concanalin A for staining of cellular membranes/endoplasmic reticulum (Perkin Elmer), with BODIPY™ 493/503 and/or with Diphenylhexatriene (DPH) for staining of neutral lipid droplets (ThermoFisher Scientific). Bright-field and fluorescence images were acquired using the confocal and non-confocal mode of the OPERA Phenix (40 x water objective) and analyses were performed on the Columbus™ system (PerkinElmer).

RT-qPCR analysis. Total RNA isolation, quality control, and reverse transcription were performed as previously described (de La Llave et al.). RT-qPCR was carried out in 384-well PCR plates (Framestar 480/384, 4titude, Dominique Dutscher) using the iTaq Universal SYBR® Green Supermix (Bio-Rad) and 0.5 µM primers with a LightCycler® 480 system (Roche Diagnostics, Meylan, France). Primer information for all targets is detailed in the supplementary table S1. Crossing Point values were determined using the second derivative maximum method (LightCycler® 480 Basic Software). The relative expression software tool (REST©-MCS) (Pfaffl et al., 2002) was used to calculate fold change (FC) values. Normalization was performed with the geometric mean of the two best reference genes Ppih and Mau2 as determined by the GeNorm and Normfinder programs (data not shown). For statistical analysis of gene expression levels, Cp values were first transformed into relative quantities (RQ) and normalized (Lecoeur et al., 2020). Nonparametric Kruskal-Wallis tests were performed on Log transformed Normalized Relative Quantity values. Results were expressed as Z-scores calculated by relative expression compared to the M0 group (short-term analyses) or the day 0 unpolarized group (long-term analyses). Heatmaps of Z-scores were generated (R, version 4.1.2) using homemade scripts based on native graphical functions.

RNASeq analysis. RNA isolation was performed with the RNeasy+ isolation kit (Qiagen) according to the manufacturer's instructions. Evaluation of RNA quality was carried out by optical density measurement using a Nanodrop device (Kisker, http://www.kisker-biotech.com) as previously described (Lecoeur et al., 2020). Total RNA was isolated from 3 independent biological replicates of uninfected and *Leishmania*-infected Mφs. DNAse Treated RNA molecules were processed for library preparation using the Truseq Stranded mRNA sample preparation kit (Illumina, San Diego, California) according to the manufacturer's instructions. An initial poly(A) RNA isolation step (included in the Illumina protocol) is performed on 1 µg

of total RNA to keep only the polyadenylated RNA fraction and remove the ribosomal RNA. A fragmentation step was performed on the enriched fraction, by divalent ions at high temperatures. The fragmented RNA samples were randomly primed for reverse transcription followed by second-strand synthesis to create double-stranded cDNA fragments. No end repair step was necessary. An adenine was added to the 3'-end and specific Illumina adapters were ligated. Ligation products were submitted to PCR amplification. The obtained oriented libraries were controlled by Bioanalyzer DNA1000 Chips (Agilent, # 5067-1504) and quantified by spectrofluorimetry (Quant-iT™ High-Sensitivity DNA Assay Kit, #Q33120, Invitrogen). Sequencing was performed on the Illumina Hiseq2500 platform to generate single-end 65 bp reads bearing strand specificity.

Reads were cleaned using cutadapt version 1.11 and only sequences at least 25 nt in length were considered for further analysis. STAR version 2.5.0a (Dobin et al., 2013), with default parameters, was used for alignment on the reference genome (GRCm38 from Ensembl database 94). Genes were counted using featureCounts version 1.4.6-p3 (Liao et al., 2014) from the Subreads package (parameters: -t gene -s 0). Transcriptomic data are made publicly available at the NCBI's Gene Expression Omnibus repository (Subseries GSE205856).

In silico analyses. “ClusterProfiler” package (version 4.2.2) of R was used for gene set enrichment analysis (GSEA) and for data mapping on metabolic pathways using the Kyoto encyclopedia of genes and genomes (KEGG) database. Results were visualized by the “enrichplot” (version 1.14.1) and the “pathview” packages (version 1.34.0). Protein-protein interaction networks were performed in Cytoscape (version 3.9.1) using STRING application (version 1.7.1). Transcription factors and targets data derived from Transcriptional regulatory relationships unravelled by sentence-based text mining (TRRUST, version 2) (Han et al., 2018),

AnimalTFDB3.0 and Riken Transcription Factor Database. A list of M1 and M2 markers was compiled from the current literature and manually curated (Jablonski et al., 2015; Orecchioni et al., 2019; Remmerie and Scott, 2018; Wang et al., 2014) (Supplementary table 2).

Statistical analyses and graphical representations. Statistics were determined by the nonparametric Wilcoxon signed-rank and Mann–Whitney U test using the GraphPad Prism 8.01 software.

RESULTS

Leishmania-infected macrophages (LIMs) show unique morphological and immunological characteristics.

In vitro LIMs were obtained by infecting bone marrow-derived Mφs (BMDMs) from C57BL/6 mice for three days with virulent, lesion-derived *Leishmania amazonensis* amastigotes (Lecoeur et al., 2020). We first assessed the morphology of *in vitro* LIMs in comparison to *in vitro* differentiated M0, M1 and M2 polarized BMDMs (see methods, and Supplementary Figures 1 and 2) (Murray, 2017). While M0 and M2 Mφs showed a similar elongated cell shape, M1 polarized cells adopted an amoeboid shape characterized by an expansion of the cytoplasm (McWhorter et al., 2013) (Fig. 1A) with a higher width/length ratio of the cells (Supplementary Figure 2) and the presence of highly refractive vesicles detectable in brightfield microscopy. These vesicles correspond to lipid droplets as demonstrated by their specific staining with BODIPY and DPH (Supplementary Figure 3). In contrast to M1 and M2 Mφs, in vitro LIMs developed a unique morphology that was defined by the absence of lipid droplets, the presence of large, parasite-containing, parasitophorous vacuoles and a highly irregular cell shape with a cellular width/length ratio similar to M0 or M2 Mφs (Fig. 1A and Supplementary Figures 2 and 3). As expected from their polarization state, we detected antimicrobial nitrite in supernatants of M1 Mφs but not in *in vitro* LIMs, M0 or M2 Mφs (Fig. 1B).

We next evaluated the expression profile by RT-qPCR of 58 genes considered as M1 or M2 markers or expressed in known anti-/pro-inflammation environments according to the current literature (Jablonski et al., 2015; Orecchioni et al., 2019; Remmerie and Scott, 2018; Wang et al., 2014). Principal components analysis (PCA) of expression changes for M1, M2 Mφs, and *in vitro* LIMs compared to M0 Mφs revealed separated clusters for each type of Mφ, suggesting unique expression profiles (Fig. 1C). Plotting the raw expression values compared to the mean

(z-score) as a heatmap confirmed the unique expression profile of *in vitro* LIMs, which can be categorized into three clusters. First, a group of genes showed an M1-like expression pattern, as judged by increased transcript abundance of for example *ccl3*, *cd68*, and *chuk* (Fig. 1D, group 1a) and reduced expression of *ccr2*, *mmp9*, and *irf4* (Fig. 1D, group 1b). Second, a group of genes that presented an M2-like expression profile, showing increased transcript abundance of *il1r1*, *dhcr24*, and *idi1* (Fig. 1D, group 2a) and reduced expression of *ccl2*, *nos2*, *il1β*, and *stat1* (Fig. 1D, group 2b). Finally, the third group of genes showed an expression profile unique for in vitro LIMs (Fig. 1D, group 3), defined by increased abundance of transcripts linked to metabolic homeostasis (e.g. *igfbp3*) (Stuard et al., 2022) and lipid metabolism (e.g. *ldlr*) (Go and Mani, 2012), the activation of sterol regulatory element-binding proteins (e.g. *insig1*) (Ouyang et al., 2020) and the biosynthesis of cholesterol (e.g. *mvd*) (Jabalquinto et al., 1988) (Fig. 1D, group 3a). Down-modulated genes (Fig. 1D group 3b) include the multifunctional inhibitor of metalloproteases TIMP1 (Grunwald et al., 2019) and key actors of the pro-inflammatory TLR/TNFR-NF-κB pathway, such as *tnfr1a*, *tlr4*, *nfκb1* and *rela*, known to be down-modulated also in *in vitro* LIMs from BALB/c mice (Lecoeur et al., 2020).

We next analyzed the morphology and the stability of the *in vitro* LIMs expression profile during long-term infection. Immunofluorescence analyses of *in vitro* LIMs at day 30 PI and *ex vivo* lesional LIMs directly recovered from footpads of infected RAG2 KO mice showed a similar, rounded cellular aspect and were filled with intracellular parasites (Fig.1 E). Applying RT-qPCR on *in vitro* LIMs at days 15 and 30 PI, and *ex vivo* LIMs revealed the long-term maintenance of the LIMs expression profile and validated their expression pattern *in situ*, as judged by high transcript abundance for *ccl3*, *igfbp3* and low transcript abundance of *irf4*, *irf5*,*cd86* when compared to M0 BMDMs (Fig. 1F).

Overall, these results reveal a highly reproducible, LIM-specific transcript profile characterized by concomitant expression of M1, M2, and unique markers that likely establish a host cell phenotype beneficial for parasite survival and multiplication.

Characterization of the *in vitro* LIMs-specific cytokine/chemokine secretion profile.

Differential cytokine and chemokine expression is a key feature of polarized Mφs (Mantovani et al., 2004; Shapouri-Moghaddam et al., 2018). To study the impact of *Leishmania* infection on the macrophage secretome, we quantified 111 cytokines, chemokines and acute phase proteins in the supernatants of M0, M1, M2 Mφs, and LIMs using a membrane-based antibody array (Supplementary Figure 4). Analysis of the global secretion pattern revealed a negative mean z-score for *in vitro* LIMs, similar to M0 cells, but distinct from M1 and M2 cells characterized by positive mean z-scores (Fig. 2A). Similar to the transcriptomic analysis, *in vitro* LIMs were characterized by the secretion of both M1 and M2 immuno-modulators as well as a unique set of proteins (Fig. 2B). 19.3% of assessed proteins in infected Mφs showed a secretion pattern similar to M1 Mφs (Fig. 2C, group 1). This group includes i) increased secretion of the pro-inflammatory factor WISP1 (Murahovschi et al., 2015) and VEGF, known to recruit monocytes and Mφs (Breen, 2007), and ii) reduced secretion of factors that limit the pathology induced by *Leishmania* infection, including FLT3L, IL5, IL22, MMP9 or EGF (Gimblet et al., 2015; Kremer et al., 2001; Montoya et al., 2018; Murahovschi et al., 2015; Murase et al., 2018; Watanabe et al., 2004).

In contrast, 42.1% of assessed proteins in *in vitro* LIMs showed a secretion pattern similar to anti-inflammatory M2 Mφs (Fig. 2C, group 2), characterized by (i) increased secretion of fibroblast growth factor (FGF) -21 known to affect glucose uptake and inhibit

macrophage-mediated inflammation (Yu et al., 2016), and (ii) absence of secretion of IL1α, IL1β, TNF, IL12p40, CXCL9 and CXCL10, all of which have been linked to resistance to *Leishmania* infection (Liew et al., 1997; Park et al., 2002; Ritter and Korner, 2002; Schleicher et al., 2016).

Finally, 38.6% of the observed expression changes were specific to *in vitro* LIMs (Fig. 2C, group 3), which can inform about immuno-regulatory pathways that are likely relevant for intracellular parasite survival. Group 3 showed reduced secretion of proteins known to restrict infection such as (i) the pro-inflammatory factors IL33 and RBP4 (Liu et al., 2017; Xu et al., 2019), (ii) activators of the inflammasome (e.g. CHEMERIN (Liang et al., 2019)), the respiratory burst (e.g. CCL2, (Rollins et al.)), the classical complement cascade (e.g. PENTRAXIN 2, (Haapasalo and Meri, 2019)), iNOS (IL33, CCL2, AHSG and CD40 (Bingaman et al., 2000; Brandonisio et al., 2002; Chattopadhyay et al., 2021; Xu et al., 2019)), (iii) drivers of the Th1 response (e.g. sRAGE, (Chen et al., 2008) and (iv) other factors known to control *Leishmania* elimination (IL3, IL7, G-CSF, and CD40) (Brandonisio et al., 2002; Gessner et al., 1993; Ho et al., 1992; Kamanaka et al., 1996; McDowell et al., 2002; Murray et al., 1995; Ritter and Moll, 2000). Conversely, Group 3 showed increased expression of molecules potentially supportive of parasite survival like (i) GAS6, an inhibitor of pro-inflammatory cytokine expression (Alciato et al., 2010), (ii) LEPTIN that inhibits NO production and increases glucose uptake and glycolytic activity (Becerril et al., 2019; Monteiro et al., 2019), and (iii) factors that favor efferocytosis (VEGF, CD93 and GAS6) (Kearns et al., 2012; Nepal et al., 2019; Norsworthy et al., 2004), which promotes an anti-inflammatory phenotype (Zhang et al., 2019).

In conclusion, *Leishmania* orchestrates a cytokine and chemokine profile that avoids host cell activation while at the same time promoting the recruitment of new monocytes or Mφs for sustained infection.

Analysis of the *in vitro* LIM-specific, bioenergetic metabolism

Given the striking metabolic differences between M1 and M2 polarized Mφs (Diskin and Palsson-McDermott, 2018; Viola et al., 2019) - respectively relying on glycolysis and oxidative phosphorylation (OXPHOS) for energy production (Russell et al., 2019) - we next assessed if the mixed immuno-phenotype of LIMs correlated to a mixed bioenergetic profile. We used a Seahorse XF Analyzer to monitor differences in glycolysis and mitochondrial respiration between M0, M1, M2 Mφs, and in vitro LIMs by measuring the extracellular acidification rate (ECAR) and the oxygen consumption rate (OCR) respectively. Basal ECAR and OCR values confirmed the polarization towards glycolysis in M1 and OXPHOS in M2 Mφs (Fig. 3A) (Van den Bossche et al., 2015). *In vitro* LIMs displayed noticeably higher oxidative respiration and glycolytic rates than M0 Mφs and overall showed a similar profile to M2 Mφs (Fig. 3A).

Next, we added a series of inhibitors to quantify respiration-dependent ATP production. The addition of the respiratory complex V inhibitor oligomycin caused a reduction in OCR values in all samples, with the strongest drop observed for M2 Mφs (Fig. 3B1). Even though LIMs showed basal OCR values similar to M2, oligomycin treatment was much less effective in reducing OCR levels, suggesting that intracellular parasites may actively sustain the host cell's respiratory functions. Complete inhibition of mitochondrial respiration in in vitro LIMs was only observed after the addition of rotenone (complex I inhibitor) and antimycin A (complex III inhibitor) (Fig. 3B1).

Inhibition of the respiratory chain usually causes a compensatory response resulting in increased glycolysis and glycolytic ATP production. Indeed, except for M1 Mφs that already rely almost completely on glycolysis, OXPHOS inhibition by oligomycin resulted in a marked increase in glycolytic activity in M0 and M2 Mφs, and *in vitro* LIMs as indicated by the elevated ECAR values (Fig. 3B2). Surprisingly, while rotenone/antimycin A treatment further enhanced the glycolytic activity in M2 Mφs, only little effect on ECAR was observed in infected Mφs. This finding suggests that intracellular parasites actively inhibit the host cell's glycolytic capacity. This suppression was further supported by two observations: first, only live but not heat-killed amastigotes caused the changes of the Mφ bioenergetic profile three days after phagocytic uptake (Supplementary Figures 5A1 and A2). Second, removal of the intracellular amastigotes with the anti-leishmanial drug Leucine-O-methyl ester (LME) (Rabinovitch and Zilberfarb, 1988) immediately released *in vitro* LIMs from their glycolytic blockage and caused an ECAR increase to levels similar to M1 Mφs (Fig. 3C1, Supplementary Figure 5B2). In contrast, LME had no or only a very minor effect on the bioenergetic read outs in M0, M1 and M2 Mφs (Fig. 3C1 and 3C2, Supplementary Fig. 5B1 and 5C1). Importantly, only anti-leishmanial LME but not the inactive control ISO-LME (Alfieri et al., 1987; Antoine et al., 1989) caused glycolytic rescue (Supplementary Figures 5D1 and D2). LME-treated *in vitro* LIMs thus show ATP production rates resulting from both glycolysis and oxidative phosphorylation similar to both M1 and M2 Mφs, respectively (Fig. 3C3).

In conclusion, our data uncover the capacity of *L. amazonensis* amastigotes to actively modulate the macrophage bioenergetic metabolism, sustaining mitochondrial but suppressing glycolytic ATP production (Fig. 3C2 and Supplementary Fig. 5C2).

The LIMs immunometabolic phenotype is under transcriptional control

We next characterized the immuno-metabolic transcript profile of *in vitro* LIMs compared to uninfected Mφs (M0) by RNAseq analysis at day 3 PI. This analysis first confirmed on genome-wide level the mixed M1/M2 phenotype of infected Mφs with numerous markers showing differential expression characteristic of both polarization states (Supplementary Fig. 6). Gene set enrichment further reproduced previous observations that *L. amazonensis* amastigotes hijack key metabolic pathways that generate nitric oxide, cholesterol or fatty acids (Osorio y Fortea et al., 2009) (Fig. 4A). In line with the observations described above, *in vitro* LIMs further show functional enrichment in the GO term 'glycolytic process' (Fig. 4A). Plotting the expression values of glycolytic genes as a heatmap (Fig. 4B) and projection of their expression ratios on the corresponding KEGG map indeed revealed upregulation of most glycolytic transcripts in LIMs (Fig. 4C), despite their glycolytic block in presence of live parasites (Fig. 3B2). Comparative RT-qPCR (Fig. 4D) and WB (Fig. 4E, Supplementary Fig. 7) analyses confirmed increased levels of transcripts and proteins for most of the glycolytic enzymes in infected Mφs compared to M0, M2 and even to M1 Mφs that present the highest glycolytic activity as judged by the ECAR values (see Fig. 3B2 and 3C1). These results lend further support to the hypothesis that glycolytic activity is suppressed in *in vitro* LIMs. In contrast, transcriptomic modulations of the PPP and the OXPHOS did not favour the use of these pathways (Supplementary figures 8 and 9). Interestingly, the transcriptomic modulations evidenced here in day 3 *in vitro* LIMs were mostly maintained in chronically infected cells, i.e. in both long- term cultured *in vitro* and *ex vivo* LIMs (Fig. 4F).

Discussion

We used a multiparametric, immuno-metabolic profiling approach to characterize in depth the phenotype of *Leishmania*-infected Mφs, termed LIMs. We uncovered a complex, atypical polarization state of *in vitro* LIMs showing idiosyncratic bioenergetic characteristics that call into question the currently prevailing notion that intracellular *Leishmania* simply triggers an M2-like phenotype while avoiding the expression of M1 marker genes (Das et al., 2021; Kumar et al., 2018; Lecoeur et al., 2020; Roy and Mandal, 2016). We have unequivocally shown that LIMs express both characteristics of M1 and M2 polarization by combining quantitative transcriptomics and proteomics analyses. This mixed Mφ expression profile correlates with the dual Th1/Th2 response observed during experimental and clinical leishmaniasis (Melby et al., 1994; Osorio et al., 2003) and with the partially characterized regulatory Mφs present in infected nodules of human diffuse cutaneous leishmaniasis (Christensen et al., 2019). Based on our results, *Leishmania* seems to manipulate the macrophage immunological profile in two complementary regulatory ways that can directly promote parasite survival and chronic infection (Fig. 5):

First, *Leishmania* infection could act in *trans* on bystander cells to actively modulate the inflammatory micro-environment and generate an external, pro-leishmanial micro-environment (Fig. 5, path A > 1). We show that in vitro LIMs indeed modulate the gene expression of many cytokines and chemokines that have profound effects on the immunological environment. On one hand, they do not secrete cytokines and chemokines that trigger anti-leishmanial Th1 response and cause Mφ activation, including IL1α, IL1β, IL,3, IL7, IL33, TNF, IL12p40, CXCL1, CXCL9, CXCL10, G-CSF, CD40, TIM1, TNF, CCL2, AHSG, soluble CD54, CD62P and RBP4 (Brandonisio et al., 2002; Chattopadhyay et al., 2021; Gessner et al., 1993; Hein and Woods, 2007; Ho et al., 1992; Jin et al., 2014; Kamanaka et al., 1996; Liew et al., 1997; Liu et al., 2017; McDowell et al., 2002; Murray et al., 1995; Ritter and Korner, 2002;

Ritter and Moll, 2000; Rollins et al., 1991; Schleicher et al., 2016; Schmal et al., 1998; Suzuki et al., 2013; Xu et al., 2019). On the other hand, they favour the secretion of factors that further attenuate the pro-inflammatory response, such as HGF, FGF21, GDF15 and GAS6 (Alciato et al., 2010; Coudriet et al., 2010; Ratnam et al., 2017; Yu et al., 2016). Paradoxically, other in vitro LIMs-secreted factors are known to promote inflammation, such as VEGF that stimulates monocyte/macrophage recruitment (Breen, 2007) and thus again supports *Leishmania* chronic infection. Finally, aside from the mixed M1/M2 expression profile, *in vitro* LIMs increased the secretion of LEPTIN which inhibits NO production (Becerril et al., 2019; Monteiro et al., 2019).

Leishmania infection also acts in *cis* and generates an internal, pro-leishmanial environment through various mechanisms (Fig. 5, path A > 2). First, the parasite modifies the macrophage transcriptome to dampen Mφ intrinsic, antimicrobial pathways avoiding the expression of genes (such as nos2) that can restrict parasite survival, and promoting the expression of genes (lipid metabolism) to satisfy the parasites' nutritional and metabolic needs and promote proliferation (Fig. 5, path A > 3). This parasite-permissive, intracellular environment is associated to an unusual bioenergetic profile that partially recapitulates the mixed M1/M2 immuno-phenotype as judged by the increase in both basal ECAR and OCR values in LIMs compared to M0 Mφs (Fig. 5, paths A4 and C). Nevertheless, based on the high oxygen consumption rate, LIMs seems to favour mitochondrial over glycolytic ATP production, showing OCR levels similar to those observed in M2 Mφs. OXPHOS in *in vitro* LIMS is further sustained by the absence (or even active inhibition) of NO production, a metabolite involved in the inhibition of mitochondrial complexes and OXPHOS (Baseler et al., 2016) (Fig. 5A5).

Surprisingly, the ECAR level in *in vitro* LIMs remained low despite the up-regulation of most glycolytic enzymes. This paradox between the expression and activity of these enzymes is compatible with a tug-of-war model between infected macrophages that recognize their

intracellular infection and are prone to mount an M1 response, and the parasite that interferes with this response to establish permissive conditions for its own survival. This model is supported by several observations: First, glycolysis and glycolytic ATP production is characteristic of M1 Mφs and supports their anti-microbial activity by promoting NADPH oxidase activity (Pavlou et al., 2017; Soto-Heredero et al., 2020). Macrophages may sense the infection and respond by increased expression of glycolytic genes. Second, only live but not heat-killed *Leishmania* affects the glycolytic pathway, revealing an active, parasite-dependent subversion mechanism. Finally, the strongest evidence for the tug-of-war model emerged from our studies with the anti-leishmanial inhibitor LME: elimination of the intracellular parasite after only 1h treatment restored high glycolytic activity in LIMs equal to M1 Mφs, thereby reaching the full glycolytic potential and matching the increased expression levels of the glycolytic enzymes. The rapidity of the response to the drug suggests that the underlying mechanism is likely transcription-independent and thus different from the transcriptomic or epigenetic immune-subversions strategies we previously reported (Lecoeur et al., 2022; Lecoeur et al., 2020). For example, the inhibition of LIMs glycolytic activity may be linked to the increased expression of *havcr2*, an immune regulator that inhibits Mφ glycolysis through Hexokinase 2 (Zhang et al., 2021), which can be inhibited by intermediate metabolites such as Glucose-6-P. In addition, other metabolites such as ATP or citrate can inhibit additional steps in the glycolytic pathway, acting on phosphofructokinase 1 and pyruvate kinase 1 (Escoll and Buchrieser, 2018; Porporato et al., 2011) (Fig. 5, path B). These metabolites may also act in concert with Mφs effectors involved in Mφ reprogramming (Noe and Mitchell, 2019) allowing real-time and constant control of the rapidly adjustable glycolysis pathway (LaManna et al., 2007).

In conclusion, our study uncovers a surprisingly complex and fine-tuned, phenotypic shift in LIMs that rules out a simple activation of the M2 polarization program. The unique

immuno-metabolic homeostasis of LIMs establishes both intracellular and extracellular conditions for parasite survival and chronic infection. Our results reveal for the first time a direct effect of these parasites on the host cell energy-producing pathways, opening a series of novel questions on the underlying molecular mechanisms and their control by parasite- or host-derived factors.

FIGURE LEGENDS

Figure 1: Phenotypic and transcriptomic characterization of LIMs. BMDMs at day 6 of *in vitro* differentiation were either treated with rm-CSF-1 alone (M0 Mφs), stimulated with LPS/IFNγ (M1 Mφs) or IL-4/IL13 (M2 Mφs), or infected with *L. am* amastigotes (LIMs). **A)** Imaging analysis. On day 3 PI, the morphology of LIMs was compared to M0, M1, and M2 Mφs using an OPERA Phenix® system. Superpositions of fluorescence images obtained with Hoechst 33342 (nuclear staining, blue) and PhenoVue™ Fluor 488/Concanavalin A (membrane staining, green) are shown. **B)** Quantitation of secreted nitrites in supernatants of Mφ cultures by Griess assay. The bars represent the standard deviation of 2 independent replicates. **C)** Principal component analysis (PCA) of the expression values of 58 transcripts for cytokines, chemokines, and NF-kB pathway members as assessed by RT-qPCR in extracts of M1 Mφs, M2 Mφs, and LIMs using the expression values of M0 Mφs as calibrators (n = 3 independent experiments). The numbers in the connecting lines indicate the distance between the three groups. **D)** Heatmap representation of the fold expression changes (z-score values) in LIMs, M1, and M2 Mφs for 58 transcripts quantified by RT-qPCR using the values of the M0 Mφ group as calibrator. Transcripts were classified according to their expression pattern into three groups that are characterized by expression changes that are shared between LIMs and M1 Mφs (group 1), shared between LIMs and M2 Mφs (group 2), or unique to LIMs (group 3). UD, undetected; a, sub-groups corresponding to transcripts showing an increased abundance in LIMs; b, sub-groups corresponding to transcripts showing decreased abundance in LIMs. **E)** Fluorescence microscopy images of *in vitro* LIMs at days 3 and 30 PI, and *ex vivo* LIMs isolated from lesions of infected RAG2 KO mice. Superpositions of fluorescence images obtained with Hoechst 33342 (nuclear staining, blue) and the mCherry signal of the transgenic parasites (red) are shown. F) Analysis of expression levels by RT-qPCR for the indicated target transcripts using total RNA extracts obtained from *in vitro* LIMs at day 3, 15 or 30 PI (n = 3 independent

experiments) and *ex vivo* lesional LIMs isolated from footpad lesions of RAG2 KO mice infected two months before (n = 4 individual mice). Values obtained from mRNA of M0 Mφs was used as calibrator. The indicated groups are defined in Fig. 1D. The grey area corresponds to unmodulated transcripts.

Figure 2: Analyte secretion pattern of in vitro LIMs, M1, and M2 Mφs. Supernatants of LIMs cultures were collected at day 3 PI and protein secretion was compared to M0, M1 and M2 Mφs using the Proteome Profiler mouse Cytokine Array Kit (n = 3 independent experiments). **A)** Violin plots showing the global changes in secretion pattern for the indicated Mφs. Z-score was computed from the signal intensity obtained for the analytes. *, $p < 0.0001$, Wilcoxon Signed-Rank test. **B)** Venn diagram. The numbers indicate analytes with overlapping secretion profiles (increase, red number; decrease, blue number). **C)** Heatmap representation of the secretion pattern shared by LIMs and M1 Mφs (group 1), LIMs and M2 Mφs (group 2) or specific to LIMS (group 3). Z-score was computed with the fold change of intensity using M0 Mφ as a calibrator.

Figure 3: Bioenergetic profiling. The analysis was performed on the different types of Mφs detailed in the legend of Fig. 1 using the Agilent Seahorse XFe96 analyzer with the Real-Time ATP Rate Assay Kit. Oxygen Consumption Rate (OCR), Extracellular Acidification Rate (ECAR), and mitochondrial and glycolytic ATP production were analyzed (n = 3 independent experiments with 5 - 8 technical replicates per plate). One representative experiment is shown. Grey, purple, green and orange colors correspond to M0, M1 and M2 Mφs, and *in vitro* LIMs, respectively. **A)** Bi-parametric dot plots of basal OCR and ECAR values for *in vitro* LIMs, M0, M1, and M2 Mφs. The ratios were calculated using the mean of the basal values obtained for

the first three time points. **B)** Kinetics of OCR (1) and ECAR (2) measurements before and after the addition of oligomycin and rotenone/antimycin A (Rot/AA). **C)** Effect of a 1-hour treatment with the anti-leishmanial drug LME on ECAR (1), OCR (2) and ATP production rate (3). Hatched bars correspond to LME-treated samples. Glycolytic ATP (glycoATP) and OXPHOS-driven ATP (mitoATP) are indicated by red and blue histograms, respectively. The Wilcoxon Mann-Whitney U test was used to determine data significance. *, $p< 0.01$; **, $p< 0.005$; ***, $p<0.001$).

Figure 4: Transcriptomic profiling analysis of *in vitro* and *ex vivo* LIMs. A) RNAseq analysis. BMDMs at day 6 of *in vitro* differentiation were either infected with *L. am* amastigotes or left untreated. Total RNA was isolated at day 3 PI from four independent biological experiments and used for RNAseq analysis. Only significantly modulated genes in in vitro LIMs (|fold change|>1.25, adjusted p-value < 0.05) were considered and subjected to metabolic pathway enrichment analysis. The number of enriched genes per GO term (yellow bars) and corresponding p values (black line) are indicated. **B)** Heatmap of z-score values obtained from transcriptomic data for modulated, glycolysis-related genes in *in vitro* LIMs compared to uninfected Mφs. **C)** Projection of expression values on a simplified KEGG map of the glycolytic pathway. Blue, reduced transcript abundance; Red, increased transcript abundance. **D)** Comparative RT-qPCR analysis of 4 glycolysis-related transcripts in the different types of Mφs at day 3 PI (see legend of Fig. 1). **E)** Comparative Western blot analysis of 4 glycolysis-related proteins in the different types of Mφs at day 3 PI (see legend of Fig.1). β-actin (ACTB) was used as a loading control. Mean ratios between integrated density values obtained for the target protein and β–actin from two independent experiments are shown in the bar plots. Fold changes were expressed using the values of the M0 Mφ sample as a calibrator. Relative protein expression was calculated by densitometric analysis using the ImageQuantTL software. **F)** RT-

qPCR analysis of *in vitro* LIMs from long-term infection and *ex vivo* LIMs obtained from infected lesions. Total RNA was isolated from control Mφs (M0), *in vitro* LIMs at day 3, 15 or 30 PI (n = 3 independent experiments) and *ex vivo* lesional Mφs (isolated from footpad lesions of RAG2 KO mice infected two months before (n = 4 individual mice). RT-qPCR was performed for a selected set of transcripts of the glycolytic pathway and the pentose phosphate pathway. All RT-qPCR data are presented in a heatmap as fold changes using *in vitro* day 0 uninfected Mφs as calibrators

Figure 5: Schematic model of the establishment of chronic internal and external pro-leishmanial environments. Amastigotes induce differential macrophage gene expression (A). They can act in *trans* on bystander cells to generate an external, pro-leishmanial micro-environment by actively modulating the secretion of M1- / M2- related cytokines and chemokines (A1). Parasites also act in *cis* to generate an internal, pro-leishmanial environment (A2) by avoiding the expression of genes that restrict parasite survival (A3), by promoting the expression of genes that satisfy the parasites' metabolic needs to permit their proliferation (A3). Finally, a tug-of-war is engaged between i) the Mϕ that recognize their intracellular infection and attempt to mount an M1 response by increasing the expression of glycolytic enzymes (A4), and ii) the parasite that interferes with this response to establish permissive conditions for its survival by dampening glycolysis (B) and increasing OXPHOS to induce an M2-like bioenergetic profile (A5, C) via still unknown parasites or Mϕ effector/ metabolites.

LEGENDS TO SUPPLEMENTARY FIGURES

Supplementary Figure 1: Determination of the optimal conditions for the generation of day 3 M1 and M2 Mφs. BMDMs at day 6 of *in vitro* differentiation were treated for 3 days to induce M1 (A) or M2 (B) Mφs. For M1 differentiation, LPS and GM-CSF were added at day 0, and IFN-γ was added at day 0 (D0) or day 2 (D2). For M2 differentiation, IL4 and IL13 and CSF-1 were added at day 0. On day 3 (A1 and B1) cell numbers were determined by counting Hoechst-stained Mφ nuclei, (A2 and B2) cell viability was assessed by counting dead cells with nuclei stained with YO-PRO-1 (dark grey bars, left Y-axis), and total RNA recovery was estimated with the NanoDrop following Macherey-Nagel™ NucleoSpin™ RNA Plus purification (light grey bars, right Y-axis). Nuclei were quantified by counting using microscopic images generated with an EVOS microscope using the 20x objective (5 fields). Mean and SEM were calculated on biological replicates (n= 3). Optimal M1 and M2 polarizing conditions used in this study are highlighted in purple (M1) and green (M2).

Supplementary Figure 2: Cell morphology of M0, M1, M2 Mφs and *in vitro* LIMs. BMDMs at day 6 of *in vitro* differentiation were incubated for 3 days in optimal polarization conditions as defined in supplementary Figure 1 to generate M0, M1, and M2 Mφs and LIMs. Cellular membranes were stained with PhenoVue™ Fluor 488 - Concanavalin A and images were acquired with a 40x objective using an OPERA Phenix system. Cell segmentation was performed with the staining before calculation of the width-to-length ratio. The violin plots represent the variation of the ratio of cell width/cell length in the indicated type of Mφ. Between 3,000 and 6,000 cells were plotted per group.

Supplementary Figure 3: Detection of lipid droplets in M0, M1, M2 Mφs and in vitro LIMs. BMDMs at day 6 of *in vitro* differentiation were incubated for 3 days in optimal polarization conditions as defined in supplementary figure 1 to generate M0, M1, M2 Mφs, and LIMs. Image acquisition was performed with the OPERA Phenix system. **A)** Lipid droplet (LD) visualization in M1 macrophages using brightfield and fluorescence microscopy. LDs were specifically stained with neutral lipid dyes DPH (blue signals) and BODIPY 493/503 (green signals). Nuclei were counterstained in blue with Hoechst 33342. Note the blue and green colocalization staining with refringent granules. **B)** LD detection using the BODIPY 493/503 neutral lipid staining (green signals) on indicated Mϕ populations. The exposition time for the BODIPY detection was defined on the M1 Mϕs population and applied to all samples.

Supplementary Figure 4: Detection of 111 analytes secreted by M0, M1, M2 Mφs and LIMs. Supernatants of M0 **(A)**, M1 **(B)**, M2 **(C)** Mφ cultures and LIMs **(D)** were harvested at day 3 PI from three independent experiments, corresponding samples were pooled, and analyzed with the Proteome Profiler Mouse Cytokine Array Kit. Analytes fixed on membranes through specific antibodies were revealed by chemiluminescence and imaging analysis was performed with the ImageQuantTL software. Membrane array design and analyte/control location are provided in the map and the table, respectively (light grey for Reference Spots; dark grey for Negative control).

Supplementary Figure 5: Impact of LME on the bioenergetic profile of *in vitro* LIMs, M0, M1 and M2 Mφs. A) Bioenergetic profiles of BMDMs analysed after 3 days of contact with heat-killed amastigotes. ECAR (A1) and OCR (A2) of one representative experiment out of two are presented. **B - E)** Analysis of the impact of LME on the bioenergetic profiles of M0,

M1 and M2 Mφs, and LIMs. ECAR **(B)** and OCR **(C)** were analyzed (n = 5 - 8 technical replicates) in real-time in the absence (basal levels) and presence of oligomycin and rotenone/antimycin A (Rot/AA). Grey, purple, and orange colors correspond to M0, M1, M2 and LIMs, respectively. The anti-leishmanial drug LME was added one hour before the analysis (dotted lines) in M0, M1 and M2 Mφs (B1, C1) and LIMs (B2, C2). **(D)** Comparison of the impact of LME and its inactive control compound ISO-Leu-O-Me after 1 hour of treatment on ECAR (D1) and OCR (D2) of LIMs. **(E)** Energetic map of the different Mφs in the absence (filled symbols) or presence (empty symbols) of LME is displayed. N = 3 independent experiments.

Supplementary Figure 6: Mixed M1-M2 profile of *in vitro* LIMs. RNAseq analysis was performed with uninfected M0 Mφs and day 3-infected LIMs (three independent biological replicates). Histograms represent the modulated M1 **(A)** and M2 **(B)** markers in LIMs versus M0 Mφs. Linear fold changes for significantly up (FC > 1.25, red color) and down (FC < -1,25, blue color) modulated genes are indicated (adjusted p-value <0.05). The list of M1 and M2 markers was defined according to the literature (see Supplementary Table 2),

Supplementary Figure 7: Detection of glycolysis enzymes by western blot. Comparative Western blot analysis of 4 glycolysis-related proteins in the different types of Mφs at day 3 PI (n = 2 technical replicates per condition). β-actin (ACTB) was used as a loading control.

Supplementary Figure 8: Simplified KEGG map representation of the pentose phosphate pathway. Day 6 BMDMs were either infected with *L. am* amastigotes or left untreated. On day 3 PI total RNA was isolated and used for RNASeq. Significantly modulated genes in LIMs

(adjusted p value < 0.05) are highlighted within the KEGG map representation of the PPP. Blue and red colors correspond to down and up modulations observed in LIMs, respectively.

Supplementary Figure 9: Bioenergetic profile of *in vitro* LIMs versus M0 macrophages. BMDMs at day 6 of *in vitro* differentiation were treated as detailed in the legend of Figure 1. RNAs were isolated on day 3 PI and RNA sequencing was performed. **A)** Profile of the running enrichment score (green line) and positions (black lines) of the gene set members of oxidative phosphorylation on the rank-ordered list. The ranking metric (Log2 fold change) is indicated (grey zone). **B)** Heatmap representing expression values (z-scores) of strongly modulated Gene Set members of the mitochondrial electron transport chain belonging to different complexes on the rank-ordered list.

LEGENDS TO SUPPLEMENTARY TABLES

Supplementary Table 1: List of primers used in RT-qPCR

The gene name, and the sequence of forward and reverse primers used in the study are indicated.

Supplementary Table 2: List of markers for M1 and M2-polarized macrophages.

[§]The list is a compilation from the literature that includes two source studies (**a**: (Orecchioni et al.); **b**: (Jablonski et al., 2015) and a manual curation (**MC**). [#] Levels of expression are indicated in the Code column (**H** for high, **L** for low, **1** for M1, **2** for M2, see insert legend).

ACKNOWLEDGEMENTS

We acknowledge the financial support of the Institut Pasteur (Paris), the Région Ile-de-France (program DIM1Health), the Institut Pasteur International Direction to the International Mixed Unit "Inflammation and *Leishmania* Infection", and the Institut national de la santé et de la recherche médicale (INSERM). Sheng Zhang is part of the Pasteur - Paris University (PPU) International PhD program. This project has received funding from the CNBG company, China.

REFERENCES

Alciato, F., Sainaghi, P.P., Sola, D., Castello, L., and Avanzi, G.C. (2010). TNF-alpha, IL-6, and IL-1 expression is inhibited by GAS6 in monocytes/macrophages. Journal of leukocyte biology *87*, 869-875.

Alfieri, S.C., Zilberfarb, V., and Rabinovitch, M. (1987). Destruction of Leishmania mexicana amazonensis amastigotes by leucine methyl ester: protection by other amino acid esters. Parasitology *95 (Pt 1)*, 31-41.

Antoine, J.C., Jouanne, C., and Ryter, A. (1989). Megasomes as the targets of leucine methyl ester in Leishmania amazonensis amastigotes. Parasitology *99 Pt 1*, 1-9.

Antonia, A.L., and Ko, D.C. (2020). Leishmaniasis: A spectrum of diseases shaped by evolutionary pressures across diverse life cycle. Evolution, medicine, and public health *2020*, 139-140.

Baseler, W.A., Davies, L.C., Quigley, L., Ridnour, L.A., Weiss, J.M., Hussain, S.P., Wink, D.A., and McVicar, D.W. (2016). Autocrine IL-10 functions as a rheostat for M1 macrophage glycolytic commitment by tuning nitric oxide production. Redox biology *10*, 12-23.

Becerril, S., Rodriguez, A., Catalan, V., Ramirez, B., Unamuno, X., Portincasa, P., Gomez-Ambrosi, J., and Fruhbeck, G. (2019). Functional Relationship between Leptin and Nitric Oxide in Metabolism. Nutrients *11*.

Bingaman, A.W., Pearson, T.C., and Larsen, C.P. (2000). The role of CD40L in T cell-dependent nitric oxide production by murine macrophages. Transplant immunology *8*, 195-202.

Bogdan, C. (2020). Macrophages as host, effector and immunoregulatory cells in leishmaniasis: Impact of tissue micro-environment and metabolism. Cytokine: X *2*, 100041.

Brandonisio, O., Panaro, M.A., Fumarola, I., Sisto, M., Leogrande, D., Acquafredda, A., Spinelli, R., and Mitolo, V. (2002). Macrophage chemotactic protein-1 and macrophage inflammatory protein-1 alpha induce nitric oxide release and enhance parasite killing in Leishmania infantum-infected human macrophages. Clinical and experimental medicine *2*, 125-129.

Breen, E.C. (2007). VEGF in biological control. Journal of cellular biochemistry *102*, 1358-1367.

Chattopadhyay, D., Das, S., Guria, S., Basu, S., and Mukherjee, S. (2021). Fetuin-A regulates adipose tissue macrophage content and activation in insulin resistant mice through MCP-1 and iNOS: involvement of IFNgamma-JAK2-STAT1 pathway. The Biochemical journal *478*, 4027-4043.

Chen, Y., Akirav, E.M., Chen, W., Henegariu, O., Moser, B., Desai, D., Shen, J.M., Webster, J.C., Andrews, R.C., Mjalli, A.M.*, et al.* (2008). RAGE ligation affects T cell activation and controls T cell differentiation. Journal of immunology *181*, 4272-4278.

Christensen, S.M., Belew, A.T., El-Sayed, N.M., Tafuri, W.L., Silveira, F.T., and Mosser, D.M. (2019). Host and parasite responses in human diffuse cutaneous leishmaniasis caused by L. amazonensis. PLoS neglected tropical diseases *13*, e0007152.

Cohen, H.B., and Mosser, D.M. (2013). Extrinsic and intrinsic control of macrophage inflammatory responses. Journal of leukocyte biology *94*, 913-919.

Coudriet, G.M., He, J., Trucco, M., Mars, W.M., and Piganelli, J.D. (2010). Hepatocyte growth factor modulates interleukin-6 production in bone marrow derived macrophages: implications for inflammatory mediated diseases. PloS one *5*, e15384.

Das, S., Mukherjee, S., and Ali, N. (2021). Super enhancer-mediated transcription of miR146a-5p drives M2 polarization during Leishmania donovani infection. PLoS pathogens *17*, e1009343.

de La Llave, E., Lecoeur, H., Besse, A., Milon, G., Prina, E., and Lang, T. (2011). A combined luciferase imaging and reverse transcription polymerase chain reaction assay for the study of Leishmania amastigote burden and correlated mouse tissue transcript fluctuations. Cellular microbiology *13*, 81-91.

Diskin, C., and Palsson-McDermott, E.M. (2018). Metabolic Modulation in Macrophage Effector Function. Frontiers in immunology *9*, 270.

Dobin, A., Davis, C.A., Schlesinger, F., Drenkow, J., Zaleski, C., Jha, S., Batut, P., Chaisson, M., and Gingeras, T.R. (2013). STAR: ultrafast universal RNA-seq aligner. Bioinformatics *29*, 15-21.
Escoll, P., and Buchrieser, C. (2018). Metabolic reprogramming of host cells upon bacterial infection: Why shift to a Warburg-like metabolism? The FEBS journal *285*, 2146-2160.
Gessner, A., Vieth, M., Will, A., Schroppel, K., and Rollinghoff, M. (1993). Interleukin-7 enhances antimicrobial activity against Leishmania major in murine macrophages. Infection and immunity *61*, 4008-4012.
Gimblet, C., Loesche, M.A., Carvalho, L., Carvalho, E.M., Grice, E.A., Artis, D., and Scott, P. (2015). IL-22 Protects against Tissue Damage during Cutaneous Leishmaniasis. PloS one *10*, e0134698.
Go, G.W., and Mani, A. (2012). Low-density lipoprotein receptor (LDLR) family orchestrates cholesterol homeostasis. The Yale journal of biology and medicine *85*, 19-28.
Grunwald, B., Schoeps, B., and Kruger, A. (2019). Recognizing the Molecular Multifunctionality and Interactome of TIMP-1. Trends in cell biology *29*, 6-19.
Haapasalo, K., and Meri, S. (2019). Regulation of the Complement System by Pentraxins. Frontiers in immunology *10*, 1750.
Han, H., Cho, J.W., Lee, S., Yun, A., Kim, H., Bae, D., Yang, S., Kim, C.Y., Lee, M., Kim, E.*, et al.* (2018). TRRUST v2: an expanded reference database of human and mouse transcriptional regulatory interactions. Nucleic acids research *46*, D380-D386.
Hein, R.M., and Woods, M.L. (2007). TIM-1 regulates macrophage cytokine production and B7 family member expression. Immunology letters *108*, 103-108.
Ho, J.L., Reed, S.G., Sobel, J., Arruda, S., He, S.H., Wick, E.A., and Grabstein, K.H. (1992). Interleukin-3 induces antimicrobial activity against Leishmania amazonensis and Trypanosoma cruzi and tumoricidal activity in human peripheral blood-derived macrophages. Infection and immunity *60*, 1984-1993.
Jabalquinto, A.M., Alvear, M., and Cardemil, E. (1988). Physiological aspects and mechanism of action of mevalonate 5-diphosphate decarboxylase. Comparative biochemistry and physiology B, Comparative biochemistry *90*, 671-677.
Jablonski, K.A., Amici, S.A., Webb, L.M., Ruiz-Rosado Jde, D., Popovich, P.G., Partida-Sanchez, S., and Guerau-de-Arellano, M. (2015). Novel Markers to Delineate Murine M1 and M2 Macrophages. PloS one *10*, e0145342.
Jin, L., Batra, S., Douda, D.N., Palaniyar, N., and Jeyaseelan, S. (2014). CXCL1 contributes to host defense in polymicrobial sepsis via modulating T cell and neutrophil functions. Journal of immunology *193*, 3549-3558.
Kamanaka, M., Yu, P., Yasui, T., Yoshida, K., Kawabe, T., Horii, T., Kishimoto, T., and Kikutani, H. (1996). Protective role of CD40 in Leishmania major infection at two distinct phases of cell-mediated immunity. Immunity *4*, 275-281.
Kearns, M.T., Dalal, S., Horstmann, S.A., Richens, T.R., Tanaka, T., Doe, J.M., Boe, D.M., Voelkel, N.F., Taraseviciene-Stewart, L., Janssen, W.J.*, et al.* (2012). Vascular endothelial growth factor enhances macrophage clearance of apoptotic cells. American journal of physiology Lung cellular and molecular physiology *302*, L711-718.
Kremer, I.B., Gould, M.P., Cooper, K.D., and Heinzel, F.P. (2001). Pretreatment with recombinant Flt3 ligand partially protects against progressive cutaneous leishmaniasis in susceptible BALB/c mice. Infection and immunity *69*, 673-680.
Kumar, A., Das, S., Mandal, A., Verma, S., Abhishek, K., Kumar, A., Kumar, V., Ghosh, A.K., and Das, P. (2018). Leishmania infection activates host mTOR for its survival by M2 macrophage polarization. Parasite immunology *40*, e12586.
LaManna, J.C., Pichiule, P., and Chavez, J. (2007). Genetics and Gene Expression of Glycolysis (Springer).
Lecoeur, H., de La Llave, E., Osorio, Y.F.J., Goyard, S., Kiefer-Biasizzo, H., Balazuc, A.M., Milon, G., Prina, E., and Lang, T. (2010). Sorting of Leishmania-bearing dendritic cells reveals subtle parasite-induced modulation of host-cell gene expression. Microbes and infection *12*, 46-54.
Lecoeur, H., Prina, E., Gutierrez-Sanchez, M., and Spath, G.F. (2022). Going ballistic: Leishmania nuclear subversion of host cell plasticity. Trends in parasitology *38*, 205-216.

Lecoeur, H., Prina, E., Rosazza, T., Kokou, K., N'Diaye, P., Aulner, N., Varet, H., Bussotti, G., Xing, Y., Milon, G.*, et al.* (2020). Targeting Macrophage Histone H3 Modification as a Leishmania Strategy to Dampen the NF-kappaB/NLRP3-Mediated Inflammatory Response. Cell reports *30*, 1870-1882 e1874.
Liang, Z., Han, L., Sun, D., Chen, Y., Wu, Q., Zhang, L., Zhou, M., and Chen, D. (2019). Chemerin-induced macrophages pyroptosis in fetal brain tissue leads to cognitive disorder in offspring of diabetic dams. Journal of neuroinflammation *16*, 226.
Liao, Y., Smyth, G.K., and Shi, W. (2014). featureCounts: an efficient general purpose program for assigning sequence reads to genomic features. Bioinformatics *30*, 923-930.
Liew, F.Y., Wei, X.Q., and Proudfoot, L. (1997). Cytokines and nitric oxide as effector molecules against parasitic infections. Philosophical transactions of the Royal Society of London Series B, Biological sciences *352*, 1311-1315.
Liu, Y., Zhong, Y., Chen, H., Wang, D., Wang, M., Ou, J.S., and Xia, M. (2017). Retinol-Binding Protein-Dependent Cholesterol Uptake Regulates Macrophage Foam Cell Formation and Promotes Atherosclerosis. Circulation *135*, 1339-1354.
Mantovani, A., Sica, A., Sozzani, S., Allavena, P., Vecchi, A., and Locati, M. (2004). The chemokine system in diverse forms of macrophage activation and polarization. Trends in immunology *25*, 677-686.
McDowell, M.A., Marovich, M., Lira, R., Braun, M., and Sacks, D. (2002). Leishmania priming of human dendritic cells for CD40 ligand-induced interleukin-12p70 secretion is strain and species dependent. Infection and immunity *70*, 3994-4001.
McWhorter, F.Y., Wang, T., Nguyen, P., Chung, T., and Liu, W.F. (2013). Modulation of macrophage phenotype by cell shape. Proceedings of the National Academy of Sciences of the United States of America *110*, 17253-17258.
Melby, P.C., Andrade-Narvaez, F.J., Darnell, B.J., Valencia-Pacheco, G., Tryon, V.V., and Palomo-Cetina, A. (1994). Increased expression of proinflammatory cytokines in chronic lesions of human cutaneous leishmaniasis. Infection and immunity *62*, 837-842.
Monteiro, L., Pereira, J., Palhinha, L., and Moraes-Vieira, P.M.M. (2019). Leptin in the regulation of the immunometabolism of adipose tissue-macrophages. Journal of leukocyte biology *106*, 703-716.
Montoya, A., Yepes, L., Bedoya, A., Henao, R., Delgado, G., Velez, I.D., and Robledo, S.M. (2018). Transforming Growth Factor Beta (TGFbeta1) and Epidermal Growth Factor (EGF) as Biomarkers of Leishmania (V) braziliensis Infection and Early Therapeutic Response in Cutaneous Leishmaniasis: Studies in Hamsters. Frontiers in cellular and infection microbiology *8*, 350.
Moreira, D., Rodrigues, V., Abengozar, M., Rivas, L., Rial, E., Laforge, M., Li, X., Foretz, M., Viollet, B., Estaquier, J.*, et al.* (2015). Leishmania infantum modulates host macrophage mitochondrial metabolism by hijacking the SIRT1-AMPK axis. PLoS pathogens *11*, e1004684.
Murahovschi, V., Pivovarova, O., Ilkavets, I., Dmitrieva, R.M., Docke, S., Keyhani-Nejad, F., Gogebakan, O., Osterhoff, M., Kemper, M., Hornemann, S.*, et al.* (2015). WISP1 is a novel adipokine linked to inflammation in obesity. Diabetes *64*, 856-866.
Murase, L.S., de Souza, J.V.P., de Lima Neto, Q.A., de Mello, T.F.P., Cardoso, B.M., Lera-Nonose, D., Teixeira, J.J.V., Lonardoni, M.V.C., and Demarchi, I.G. (2018). The role of metalloproteases in Leishmania species infection in the New World: a systematic review. Parasitology *145*, 1499-1509.
Murray, H.W., Cervia, J.S., Hariprashad, J., Taylor, A.P., Stoeckle, M.Y., and Hockman, H. (1995). Effect of granulocyte-macrophage colony-stimulating factor in experimental visceral leishmaniasis. The Journal of clinical investigation *95*, 1183-1192.
Murray, P.J. (2017). Macrophage Polarization. Annual review of physiology *79*, 541-566.
Nepal, S., Tiruppathi, C., Tsukasaki, Y., Farahany, J., Mittal, M., Rehman, J., Prockop, D.J., and Malik, A.B. (2019). STAT6 induces expression of Gas6 in macrophages to clear apoptotic neutrophils and resolve inflammation. Proceedings of the National Academy of Sciences of the United States of America *116*, 16513-16518.
Noe, J.T., and Mitchell, R.A. (2019). Tricarboxylic acid cycle metabolites in the control of macrophage activation and effector phenotypes. Journal of leukocyte biology *106*, 359-367.

Norsworthy, P.J., Fossati-Jimack, L., Cortes-Hernandez, J., Taylor, P.R., Bygrave, A.E., Thompson, R.D., Nourshargh, S., Walport, M.J., and Botto, M. (2004). Murine CD93 (C1qRp) contributes to the removal of apoptotic cells in vivo but is not required for C1q-mediated enhancement of phagocytosis. Journal of immunology *172*, 3406-3414.
O'Neill, L.A., Kishton, R.J., and Rathmell, J. (2016). A guide to immunometabolism for immunologists. Nature reviews Immunology *16*, 553-565.
Orecchioni, M., Ghosheh, Y., Pramod, A.B., and Ley, K. (2019). Macrophage Polarization: Different Gene Signatures in M1(LPS+) vs. Classically and M2(LPS-) vs. Alternatively Activated Macrophages. Frontiers in immunology *10*, 1084.
Osorio y Fortea, J., de La Llave, E., Regnault, B., Coppee, J.Y., Milon, G., Lang, T., and Prina, E. (2009). Transcriptional signatures of BALB/c mouse macrophages housing multiplying Leishmania amazonensis amastigotes. BMC genomics *10*, 119.
Osorio, Y., Melby, P.C., Pirmez, C., Chandrasekar, B., Guarin, N., and Travi, B.L. (2003). The site of cutaneous infection influences the immunological response and clinical outcome of hamsters infected with Leishmania panamensis. Parasite immunology *25*, 139-148.
Ouyang, S., Mo, Z., Sun, S., Yin, K., and Lv, Y. (2020). Emerging role of Insig-1 in lipid metabolism and lipid disorders. Clinica chimica acta; international journal of clinical chemistry *508*, 206-212.
Park, A.Y., Hondowicz, B., Kopf, M., and Scott, P. (2002). The role of IL-12 in maintaining resistance to Leishmania major. Journal of immunology *168*, 5771-5777.
Pavlou, S., Wang, L., Xu, H., and Chen, M. (2017). Higher phagocytic activity of thioglycollate-elicited peritoneal macrophages is related to metabolic status of the cells. Journal of inflammation *14*, 4.
Pfaffl, M.W., Horgan, G.W., and Dempfle, L. (2002). Relative expression software tool (REST) for group-wise comparison and statistical analysis of relative expression results in real-time PCR. Nucleic acids research *30*, e36.
Porporato, P.E., Dhup, S., Dadhich, R.K., Copetti, T., and Sonveaux, P. (2011). Anticancer targets in the glycolytic metabolism of tumors: a comprehensive review. Frontiers in pharmacology *2*, 49.
Rabhi, I., Rabhi, S., Ben-Othman, R., Rasche, A., Daskalaki, A., Trentin, B., Piquemal, D., Regnault, B., Descoteaux, A., Guizani-Tabbane, L*., et al.* (2012). Transcriptomic signature of Leishmania infected mice macrophages: a metabolic point of view. PLoS neglected tropical diseases *6*, e1763.
Rabinovitch, M., and Zilberfarb, V. (1988). Destruction of intracellular and isolated Leishmania mexicana amazonensis amastigotes by amino acid amides. Parasitology *96 (Pt 2)*, 289-296.
Ratnam, N.M., Peterson, J.M., Talbert, E.E., Ladner, K.J., Rajasekera, P.V., Schmidt, C.R., Dillhoff, M.E., Swanson, B.J., Haverick, E., Kladney, R.D*., et al.* (2017). NF-kappaB regulates GDF-15 to suppress macrophage surveillance during early tumor development. The Journal of clinical investigation *127*, 3796-3809.
Remmerie, A., and Scott, C.L. (2018). Macrophages and lipid metabolism. Cellular immunology *330*, 27-42.
Ritter, U., and Korner, H. (2002). Divergent expression of inflammatory dermal chemokines in cutaneous leishmaniasis. Parasite immunology *24*, 295-301.
Ritter, U., and Moll, H. (2000). Monocyte chemotactic protein-1 stimulates the killing of leishmania major by human monocytes, acts synergistically with IFN-gamma and is antagonized by IL-4. European journal of immunology *30*, 3111-3120.
Rodriguez, N.E., Lockard, R.D., Turcotte, E.A., Araujo-Santos, T., Bozza, P.T., Borges, V.M., and Wilson, M.E. (2017). Lipid bodies accumulation in Leishmania infantum-infected C57BL/6 macrophages. Parasite immunology *39*.
Rollins, B.J., Walz, A., and Baggiolini, M. (1991). Recombinant human MCP-1/JE induces chemotaxis, calcium flux, and the respiratory burst in human monocytes. Blood *78*, 1112-1116.
Roy, S., and Mandal, C. (2016). Leishmania donovani Utilize Sialic Acids for Binding and Phagocytosis in the Macrophages through Selective Utilization of Siglecs and Impair the Innate Immune Arm. PLoS neglected tropical diseases *10*, e0004904.
Russell, D.G., Huang, L., and VanderVen, B.C. (2019). Immunometabolism at the interface between macrophages and pathogens. Nature reviews Immunology *19*, 291-304.

Schleicher, U., Paduch, K., Debus, A., Obermeyer, S., Konig, T., Kling, J.C., Ribechini, E., Dudziak, D., Mougiakakos, D., Murray, P.J.*, et al.* (2016). TNF-Mediated Restriction of Arginase 1 Expression in Myeloid Cells Triggers Type 2 NO Synthase Activity at the Site of Infection. Cell reports *15*, 1062-1075.
Schmal, H., Czermak, B.J., Lentsch, A.B., Bless, N.M., Beck-Schimmer, B., Friedl, H.P., and Ward, P.A. (1998). Soluble ICAM-1 activates lung macrophages and enhances lung injury. Journal of immunology *161*, 3685-3693.
Shapouri-Moghaddam, A., Mohammadian, S., Vazini, H., Taghadosi, M., Esmaeili, S.A., Mardani, F., Seifi, B., Mohammadi, A., Afshari, J.T., and Sahebkar, A. (2018). Macrophage plasticity, polarization, and function in health and disease. Journal of cellular physiology *233*, 6425-6440.
Shinkai, Y., Rathbun, G., Lam, K.P., Oltz, E.M., Stewart, V., Mendelsohn, M., Charron, J., Datta, M., Young, F., Stall, A.M.*, et al.* (1992). RAG-2-deficient mice lack mature lymphocytes owing to inability to initiate V(D)J rearrangement. Cell *68*, 855-867.
Soto-Heredero, G., Gomez de Las Heras, M.M., Gabande-Rodriguez, E., Oller, J., and Mittelbrunn, M. (2020). Glycolysis - a key player in the inflammatory response. The FEBS journal *287*, 3350-3369.
Stuard, W.L., Titone, R., and Robertson, D.M. (2022). IGFBP-3 functions as a molecular switch that mediates mitochondrial and metabolic homeostasis. FASEB journal : official publication of the Federation of American Societies for Experimental Biology *36*, e22062.
Suzuki, J., Hamada, E., Shodai, T., Kamoshida, G., Kudo, S., Itoh, S., Koike, J., Nagata, K., Irimura, T., and Tsuji, T. (2013). Cytokine secretion from human monocytes potentiated by P-selectin-mediated cell adhesion. International archives of allergy and immunology *160*, 152-160.
Ty, M.C., Loke, P., Alberola, J., Rodriguez, A., and Rodriguez-Cortes, A. (2019). Immuno-metabolic profile of human macrophages after Leishmania and Trypanosoma cruzi infection. PloS one *14*, e0225588.
Van den Bossche, J., Baardman, J., and de Winther, M.P. (2015). Metabolic Characterization of Polarized M1 and M2 Bone Marrow-derived Macrophages Using Real-time Extracellular Flux Analysis. Journal of visualized experiments : JoVE.
Viola, A., Munari, F., Sanchez-Rodriguez, R., Scolaro, T., and Castegna, A. (2019). The Metabolic Signature of Macrophage Responses. Frontiers in immunology *10*, 1462.
Wang, N., Liang, H., and Zen, K. (2014). Molecular mechanisms that influence the macrophage m1-m2 polarization balance. Frontiers in immunology *5*, 614.
Watanabe, Y., Hamaguchi-Tsuru, E., Morimoto, N., Nishio, Y., Yagyu, K., Konishi, Y., Tominaga, M., Miyazaki, J., Furuya, M., and Tominaga, A. (2004). IL-5-Induced Eosinophils Suppress the Growth of Leishmania amazonensis In Vivo and Kill Promastigotes In Vitro in Response to Either IL-4 or IFN-gamma. DNA and cell biology *23*, 412-418.
Xu, H., Sun, L., He, Y., Yuan, X., Niu, J., Su, J., and Li, D. (2019). Deficiency in IL-33/ST2 Axis Reshapes Mitochondrial Metabolism in Lipopolysaccharide-Stimulated Macrophages. Frontiers in immunology *10*, 127.
Yu, Y., He, J., Li, S., Song, L., Guo, X., Yao, W., Zou, D., Gao, X., Liu, Y., Bai, F.*, et al.* (2016). Fibroblast growth factor 21 (FGF21) inhibits macrophage-mediated inflammation by activating Nrf2 and suppressing the NF-kappaB signaling pathway. International immunopharmacology *38*, 144-152.
Zhang, J., Hou, C., Dou, S., Li, G., Wang, Z., Liu, Y., Zhang, Y., Wang, R., Shen, B., and Han, G. (2021). T cell immunoglobulin and mucin domain protein 3 inhibits glycolysis in RAW 264.7 macrophages through Hexokinase 2. Scandinavian journal of immunology *93*, e12981.
Zhang, S., Weinberg, S., DeBerge, M., Gainullina, A., Schipma, M., Kinchen, J.M., Ben-Sahra, I., Gius, D.R., Yvan-Charvet, L., Chandel, N.S.*, et al.* (2019). Efferocytosis Fuels Requirements of Fatty Acid Oxidation and the Electron Transport Chain to Polarize Macrophages for Tissue Repair. Cell metabolism *29*, 443-456 e445.

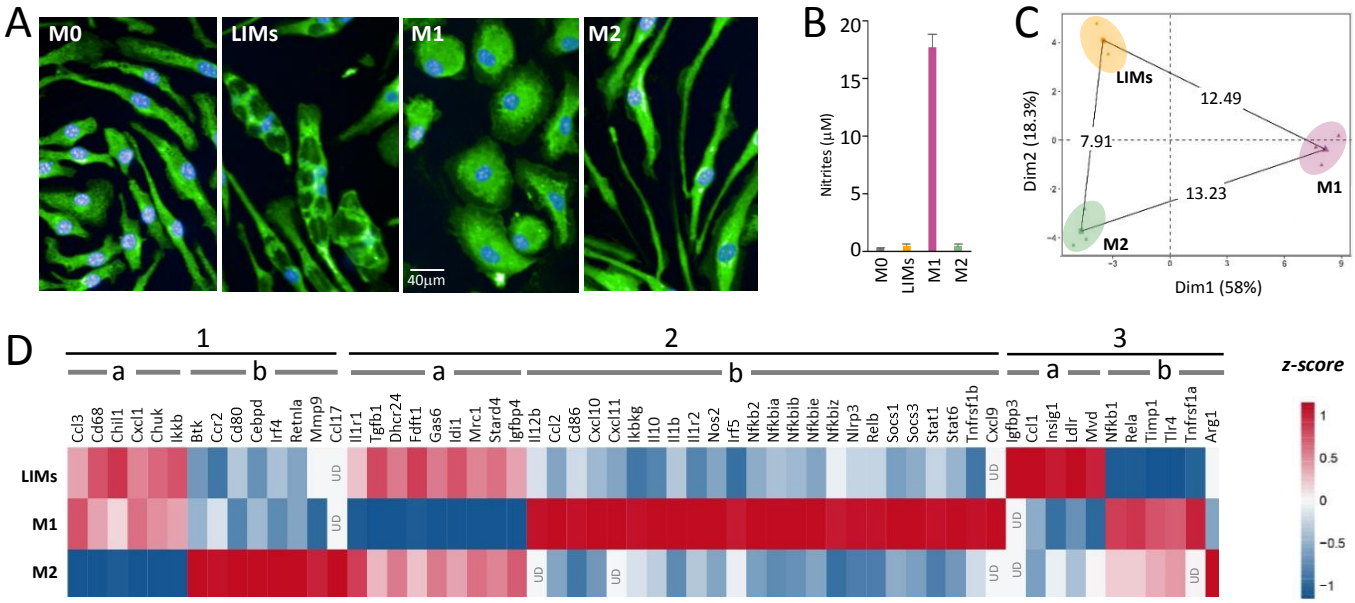

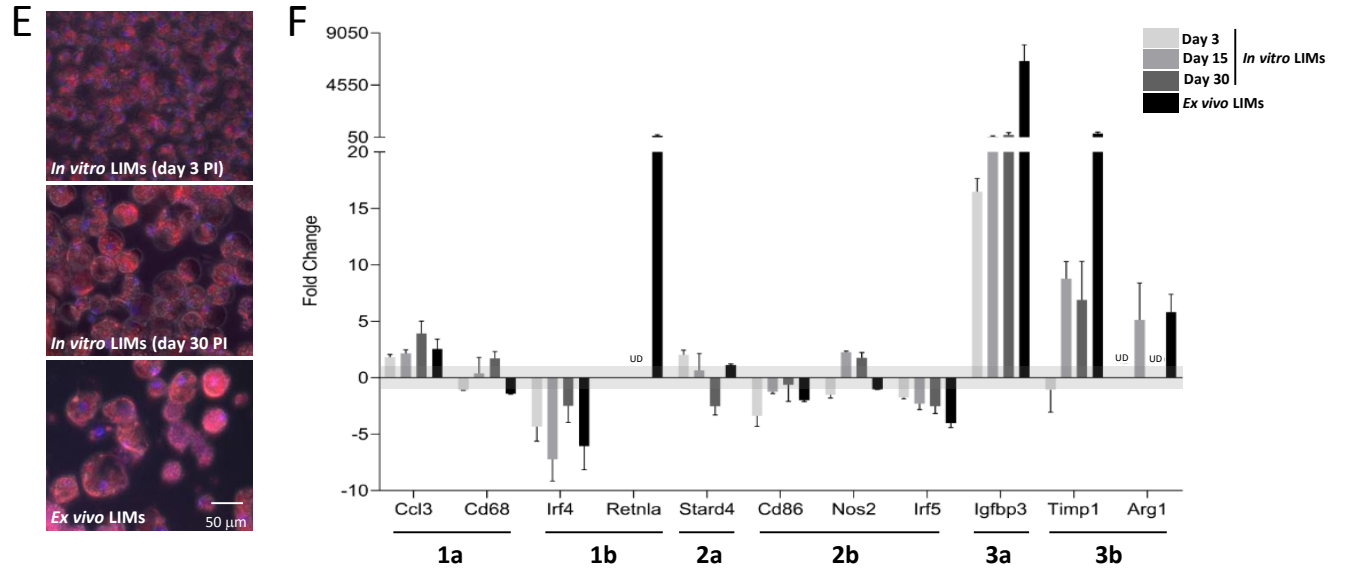

Figure 1, Zhang et al.

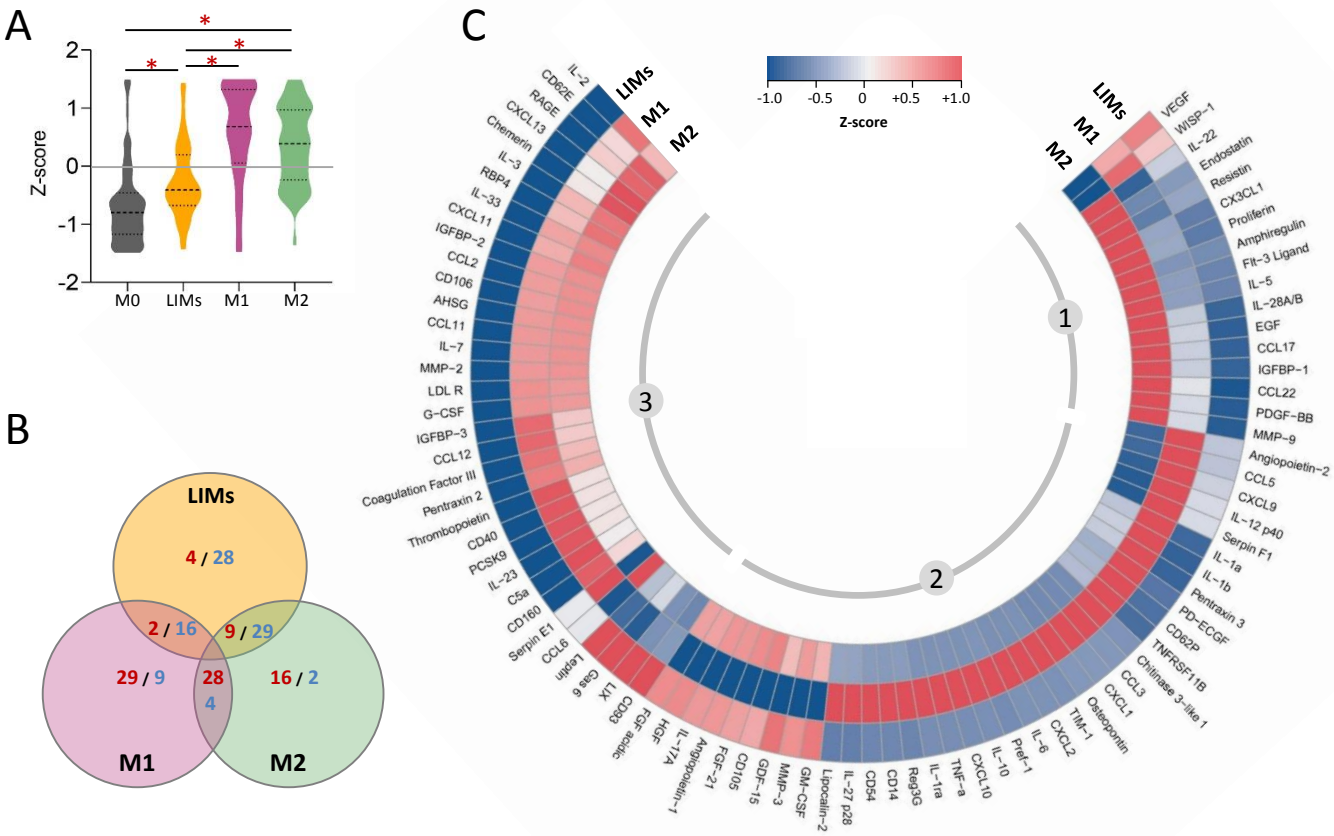

Figure 2, Zhang et al.

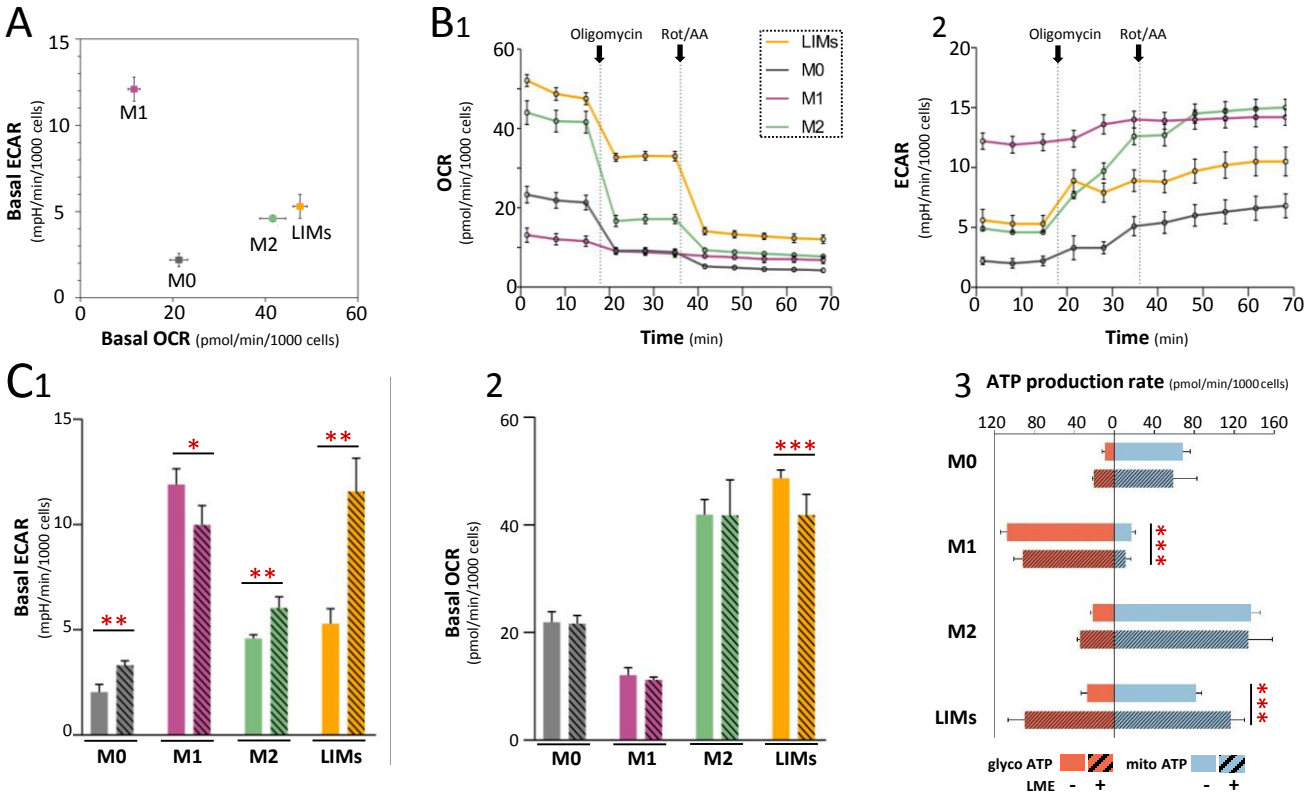

Figure 3, Zhang et al.

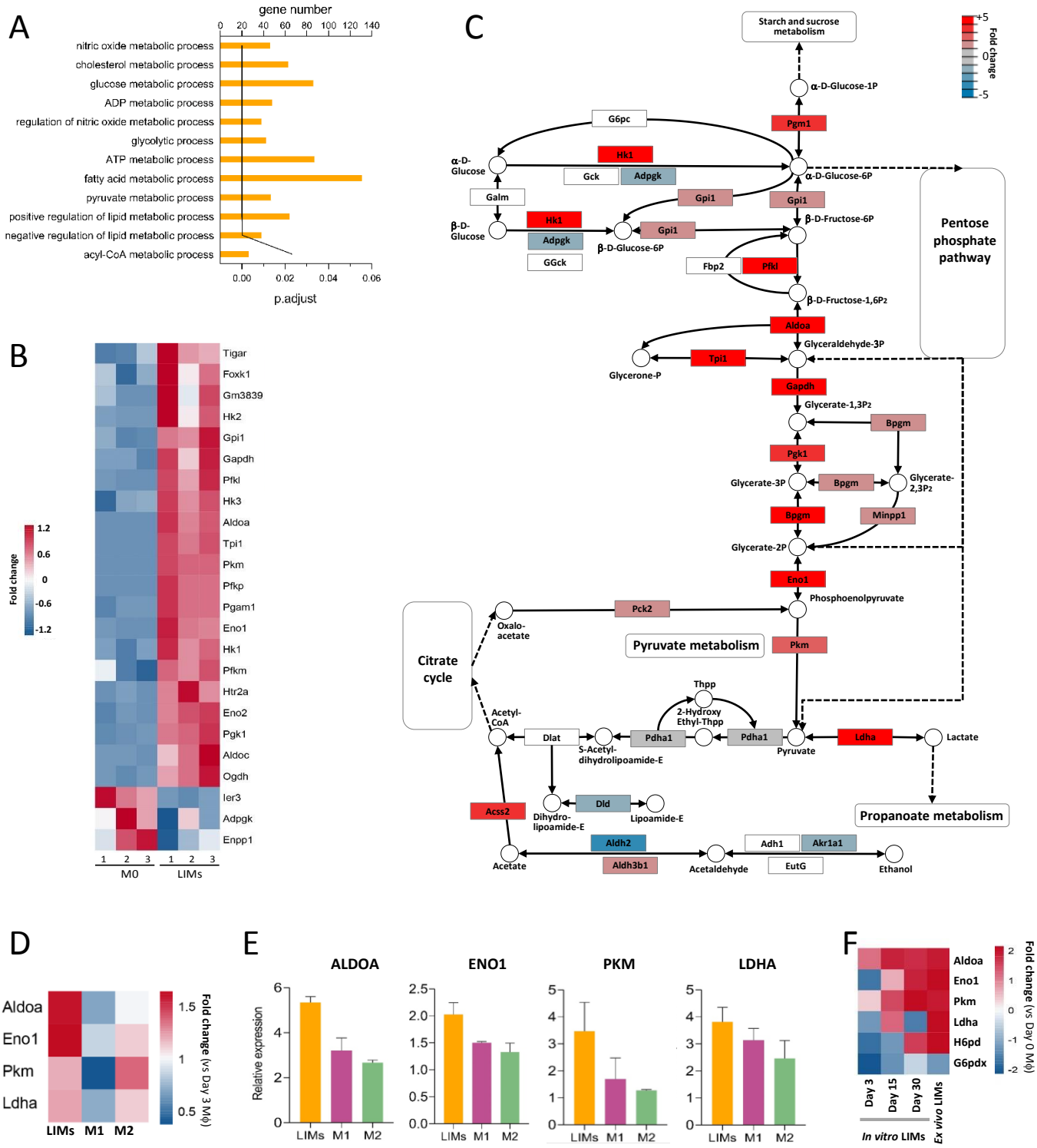

Figure 4, Zhang et al.

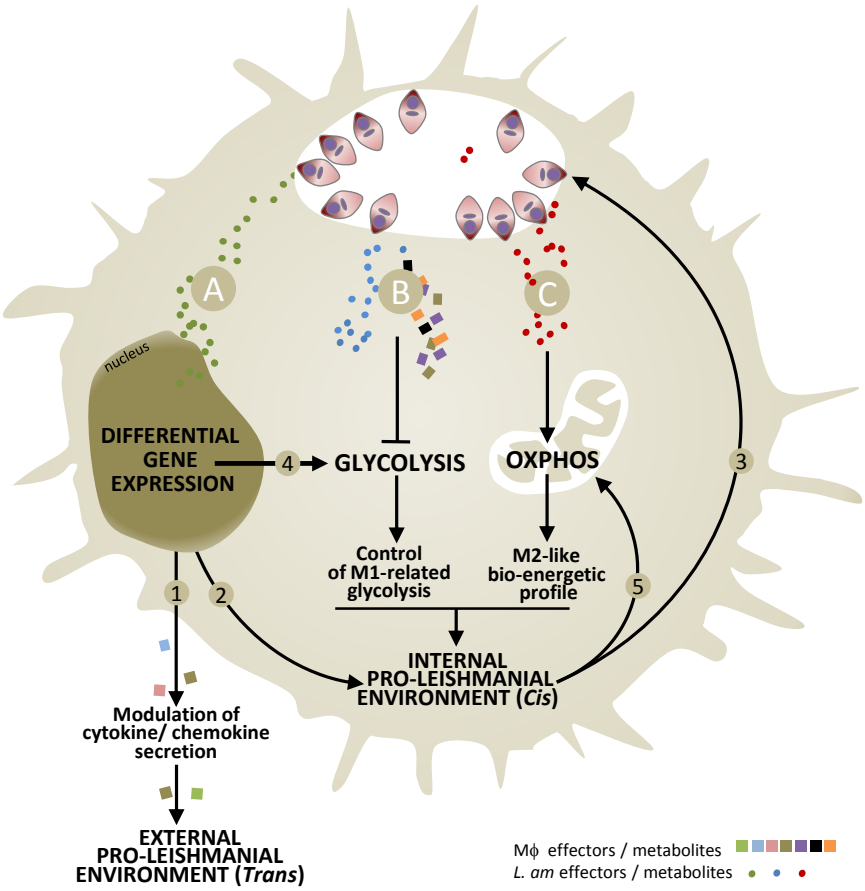

Figure 5, Zhang et al.